Submitted for publication in The International Journal of Robotics Research

Experiments in Control of a Flexible-Link Robotic Manipulator with Unknown Payload Dynamics: *An Adaptive Approach*

Lawrence J. Alder* Stephen M. Rock †

Stanford University Aerospace Robotics Laboratory
Stanford, California 94305

September 27, 1993

Abstract— This paper presents technology that extends the concept of end-point control of a flexible-link robot arm to handle payloads with unknown internal dynamics. The approach is based on merging high-performance control with an innovative identification algorithm in a self-tuning regulator framework. Payload dynamics are identified in real-time using recently developed subspace fitting techniques. Sufficient excitation issues are addressed. End-point feedback controllers are formulated using frequency weighted linear quadratic gaussian design methods.

Experimental results demonstrating precision control of a very flexible single-link robot arm with unknown dynamic payloads are presented.

1 Introduction

Space based robots such as the shuttle Remote Manipulator System (RMS) and the proposed Space Station Remote Manipulator System (SSRMS) have been and will be essential elements of future space exploration systems. These robots will provide the capability to perform precise positioning of various payloads (e.g., docking of satellites, assembly of structures and modules, etc.). Achieving precision control of such tasks will be difficult. The manipulators will necessarily be long and light weight, and the payloads of interest will potentially be massive. As a consequence, structural flexibility in the manipulator links will be unavoidable and significant. Further, the manipulated payloads will possibly include unknown internal dynamics. Examples include sloshing fuel and/or flexible appendages (e.g., vibrating solar panels on a small satellite).

The body of control research that has been reported previously for flexible-link space robotic manipulators is insufficient to achieve high-performance end-point control of such complex configurations. Some researchers have successfully used feedforward techniques such as input shaping [1] and inverse dynamics [2] to command motion of flexible-link systems. These techniques work effectively when the plant model is known and the state of the system is known. However, they provide no regulation or disturbance rejection.

Regulation and disturbance rejection are provided by feedback. Collocated feedback controllers have been proposed as a scheme that is insensitive to payload dynamics, but they have been shown to yield low-performance end-point control [3]. High-performance end-point control has been achieved and demonstrated experimentally using non-collocated controllers [3], but only for configurations involving payloads that were well modeled by a tip inertia matrix only. In addition, these high-performance non-collocated controllers have been shown to be sensitive to the mass and inertia of the tip [4] (a controller that is tuned for a particular tip mass may in fact be unstable for a different tip mass). Finally, the sensitivity to unknown tip mass has been addressed successfully using adaptive endpoint control [5], but the approach did not account for unknown payload dynamics.

The goal of this research is to develop a feedback control technique that provides precise, high-bandwidth endpoint control of a flexible-link manipulator and simultaneously damps any internal oscillations of its payload. This is to be accomplished for configurations in which the internal dynamics of the payload are not known apriori and cannot be sensed directly. The only sensors used for con-

*Ph.D. Department of Aeronautics and Astronautics.
†Associate Professor, Dept. of Aeronautics and Astronautics.

trol will be part of the main robotic arm[1]. It is assumed that it will not be practical to outfit the payload with sensors that measure its internal state.

The control approach that is developed and demonstrated experimentally in this paper is based on extensions to the self-tuning regulator solution of adaptive control. Although other researchers have explored self-tuning regulators for the control of flexible-link robotic manipulators ([5]-[8]), their work has focused on identifying a complete robot assembly assuming that the payload is known to be a rigid body. One group [9] addressed the issue of payload dynamics but only from the standpoint of low-performance robust control. Their approach is to separate the control of the arm and payload by controlling the arm to be a virtual force source. However, their controller is limited to bandwidths less than any structural flexibility of the manipulator: payloads with dynamic modes above this low-control bandwidth are not actively damped. No simulation or experimental results are presented in their paper.

In the research presented here, even though payload dynamics are unknown apriori, flexibility in both the arm and payload is accounted for by active control. This is experimentally demonstrated for a case where the payload natural frequencies are up to an order of magnitude above the first cantilever flexible mode frequency of the robot arm. In order to achieve this, the approach presented here exploits various attributes of a class of systems that will be typical of some deployed space robots. It yields a feasible, real-time control that potentially could be implemented in space.

2 Class of Systems

The configuration addressed in this research is a single very flexible-link arm that is grasping an object which contains a single degree-of-freedom pendulum. The pendulum length is adjustable. This system is characteristic of a future space-based manipulator that is grasping a satellite with unknown internal dynamics (e.g., sloshing fuel). This configuration is ideal for basic control studies since it has minimum complexity yet exhibits all of the fundamental problems associated with control.

Experimental Apparatus

Figure 1 shows a schematic diagram of the hardware which was designed and constructed. Its robotic arm is a flexible beam which moves in the horizontal plane. A torque motor drives one end of the beam and a payload is attached to the other. The payload is supported on a pad that floats on an airbearing over a smooth granite table (this simulates the zero-g environment of space in one dimension). The pad and air bearing also prevent out of plane vibrations. The pad has a pendulum mounted on it that represents the dynamic payload.

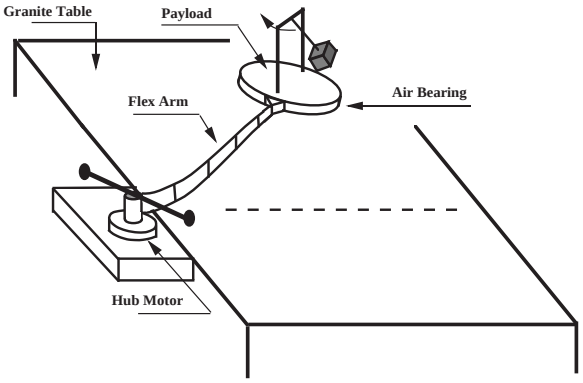

Figure 1: **Experimental System**

This is a schematic of the experimental apparatus. A single-link flexible beam with a payload floats on a granite table to simulate zero-g. The payload has internal dynamics in the form of a pendulum.

The payload pendulum can be locked mechanically, or it can be set free to oscillate. Further, the length of the pendulum can be varied. This allows control performance for a range of "unknown" frequencies of oscillation to be investigated. The damping ratio associated with of the free motion of the pendulum is on the order of 0.5% (when released from a 45^o initial condition, it takes about one minute to damp within $\pm 5^o$ of its steady-state value).

Figure 2 shows the sensors and actuators that have been incorporated. There are angle and rate sensors at the hub, and there is a camera mounted to the ceiling that senses position and orientation of the payload. There is also a limited angle torque motor at the hub.

Note that this suite of sensors was designed to generate a set of data typical of that which could be available in a deployed robotic system. In particular, the overhead vision system provides the same basic information that would be available from a local Global Positioning System (GPS). That is, the critical feature of this sensor is its ability to measure the end-point position of the manipulator.

Measurement of the pendulum angle is also provided, but this signal is used for data collection only. It is not used for control or identification since it is assumed that such instrumentation will not be available in deployed systems.

Reference [10] has a more detailed description of the hardware including mass properties.

[1] This includes sensing of the end-point

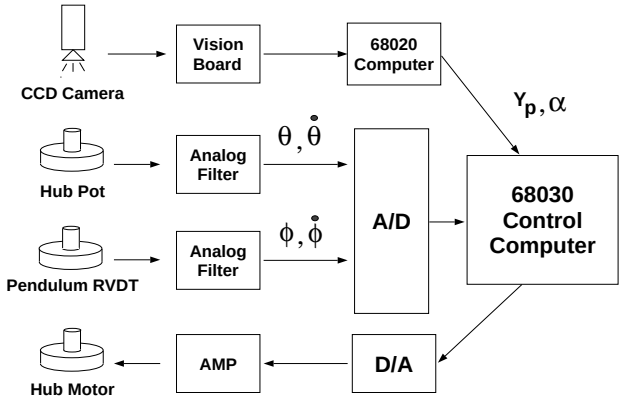

Figure 2: **I/O Schematic**

See Figures 3 and 4 for a definition of the symbols: Y_p, α, θ, and ϕ.

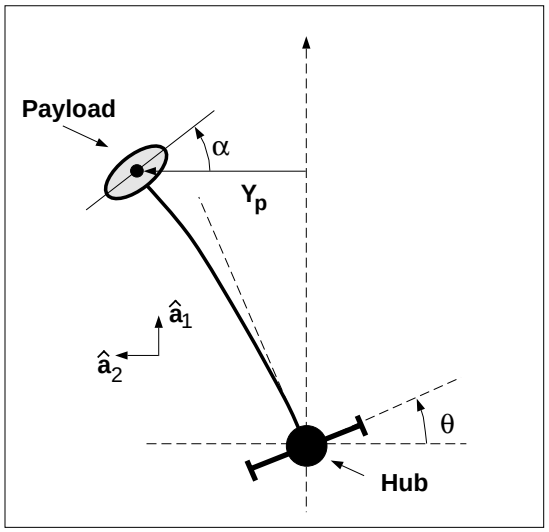

Figure 3: **Manipulator Top View**

This shows the payload position (Y_p), payload orientation (α), and hub angle (θ).

Equations of Motion

The linearized equations of motion of this system can be expressed as (see [11]):

$$\dot{x} = Ax + Bu + , w \ , \quad (1)$$

$$y_c = C_c x \ , \quad (2)$$

$$y_s = C_s x + v \ , \quad (3)$$

where x is the state vector, u is the control vector, w is the process disturbance vector , y_c is the vector of outputs of interest, y_s is the vector of measured or sensed outputs and v is the measurement noise vector. The matrix A is the plant dynamics matrix, and B, , , C_c, and C_s are distribution matrices. These equations depend on the dynamics of the payload. For the experimental system, the sensed outputs are:

$$y_s = \left[\begin{array}{l} Payload\,Position \ \ (Y_p), \\ Payload\,Orientation \ \ (\alpha), \\ Hub\,Rate \ \ (\dot{\theta}) \end{array} \right]. \quad (4)$$

where the *Payload Position*, Y_p, is defined as the perpendicular distance from the center line of the table to the geometric center of the payload. The *Payload Orientation*, α, is defined as the orientation of the payload pad with respect to the granite surface. The outputs that are to be controlled, y_c, include the position and orientation of the payload as well as the payload internal states (if they exist). Figures 3 and 4 show the physical significance the symbols Y_p, α, θ, and ϕ.

The equations of motion for the experimental systems were generated by first measuring its mass and geometric properties and then using a finite-element technique. The order of the model was reduced using modal truncation. Reference [11] provides the details of how the model was generated as well as validation of the model against experimental data. Appendix A gives the numerical values of matrices A, B, etc. for both a rigid-body and one dynamic payload configuration.

When the pendulum is locked, the first three natural frequencies of the system are 1.4 Hz, 3.4 Hz and 8.7 Hz. When the pendulum is set free, an additional natural mode appears between 1.5-2.5 Hz depending on the pendulum length that is set. The original three modal frequencies change only slightly.

The mode shapes and frequencies for the rigid and dynamic payload cases are presented in Figures 5 and 6 for two different pendulum lengths. Figure 5 shows the case where the pendulum is a factor of three shorter than

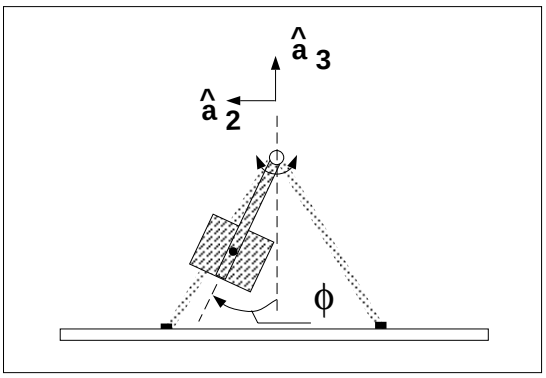

Figure 4: **Payload Front View**

This figure shows the pendulum angle (ϕ).

the case shown in Figure 6. The natural frequencies are labelled "ω_{loc}" for the case where the payload is rigid and "ω_{dyn}" if the pendulum is free. The "pendulum-locked" mode shapes are shown with a solid line and the "pendulum-free" mode shapes are shown dotted.

An observation is that for three system modes neither their shapes nor their frequencies are strongly affected by the presence of the pendulum. The main effect of releasing the pendulum is to introduce a new mode into the system.

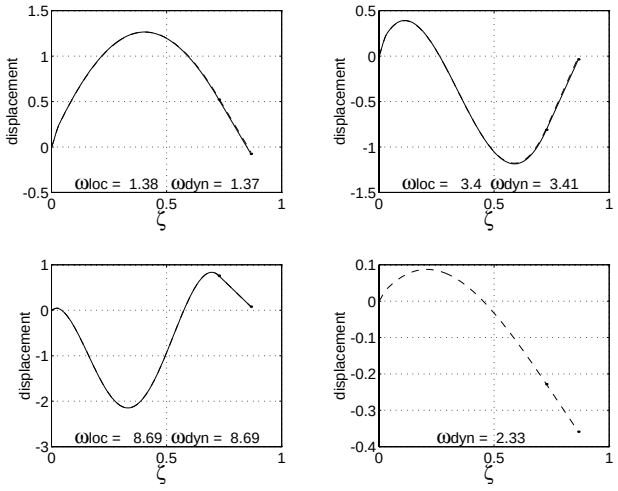

Figure 5: **Mode Shapes**

The solid lines are the mode shapes for the pendulum locked. The dashed lines are for the pendulum unlocked. ζ is the normalized length along the axis of the arm. The mode shape shown in the lower right corner is only present when the pendulum is free. Note that three of the modes are virtually unchanged in frequency and shape by the presence of the dynamic payload.

This relative insensitivity of a subset of the mode shapes and frequencies to variations in pendulum length is a property of the system that is exploited in developing the adaptive control solution in the sections that follow.

3 Control Approach

Previous work has demonstrated that high-performance end-point control of flexible-link robotic systems is achievable using linear quadratic gaussian (LQG) design techniques, but only if an accurate model of the system (robot plus payload) is available [3]. Systems that are typical of future space robotic applications do not meet this requirement. Although it is likely that an accurate model of the manipulator exists over the frequency range of the vibration modes to be controlled actively, there are at least

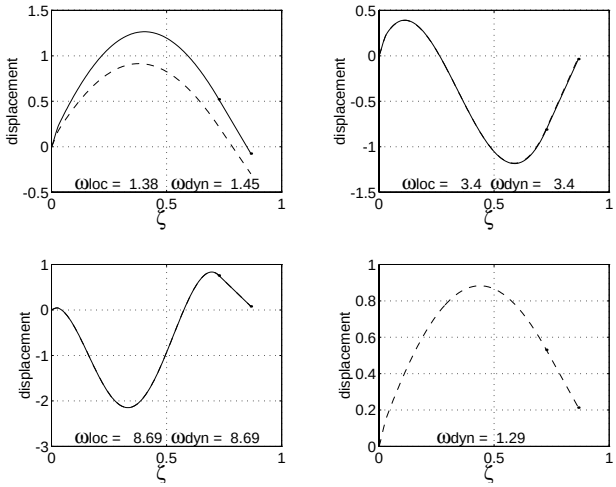

Figure 6: **Mode Shapes - Highly Coupled Case**

The solid line is the mode shapes for the pendulum locked. The dashed line is for the pendulum unlocked. ζ is the normalized length along the axis of the arm. This case shows that the first mode is coupled to the pendulum.

two types of modelling error that must be accounted for in the control design process. The first is the presence of "unknown" dynamics in the payload. The second is the presence of high-frequency modelling errors in the arm itself and in the sensing/actuation system. For the experimental apparatus, the unknown dynamics result from the pendulum. The dominant high-frequency uncertainties result from time delays in the sensing system (the delay is a result of the 30 milliseconds that it takes for the vision board and computer, shown in Figure 2, to process a frame of vision data).

The goal of this research is to develop a control design approach that will account for these modelling uncertainties and errors. The approach taken is to merge the frequency-shaping concepts of robust control with the adaptive features of the self-tuning regulator. The objective is to be robust to the high-frequency uncertainties of the arm and adapt to the unknown dynamics in the payload. Further, the procedure is based on exploiting attributes of the class of systems considered in order to produce a control law that will potentially be implementable in more complex configurations.

This section focuses on the design of an LQG based controller that is robust to the high frequency uncertainties. The next section incorporates the adaptive features.

Presented first is an overview of how the LQG design procedure is modified to include frequency-shaping of the cost function to account for the high-frequency modelling errors and the sensor system delays. "Robust" controllers are developed for both locked-pendulum (rigid)

and free-pendulum (dynamic) configurations. For these cases, the characteristics of the payload pendulum are assumed known.

The results demonstrate that the robust control can yield high levels of performance in the presence of high-frequency uncertainties if the payload model is known. It is then shown, however, that the performance of these controllers is poor or even unstable in the face of the payload parameter uncertainties. This provides the justification for an adaptive system that identifies a payload model as part of the control system. This adaptive system is discussed in the subsequent sections.

Frequency-Shaped Control Design

The procedure incorporated here for designing a control system that is insensitive to unmodelled high-frequency dynamics is based on the well known concept of frequency shaping. A controller is designed by minimizing a frequency weighted cost function [12]

$$J = E\left[\int_{-\infty}^{\infty} [y_c(j\omega)^T Q(j\omega) y_c(j\omega) + u(j\omega)^T R(j\omega) u(j\omega)] d\omega\right] \quad (5)$$

where y_c are the outputs that are to be controlled (not necessarily measured), u are the available controls, and $Q(j\omega)$ and $R(j\omega)$ are the frequency dependent weighting matrices. The cost function is minimized subject to the linearized, time-invariant, state-space equations of motion that describe the arm and payload (Equations 1 through 3). The cost function is driven by the process and measurement disturbances which are assumed to be gaussian white noise:

$$w_a \equiv \begin{bmatrix} w \\ v \end{bmatrix}, \quad (6)$$

$$E[w_a(t)] = 0, \quad (7)$$

$$E[w_a(t) w_a^T(t')] = Q_{n_a} \delta(t - t'), \quad (8)$$

$$Q_{n_a} \equiv \begin{bmatrix} Q_n & 0 \\ 0 & R_n \end{bmatrix}, \quad (9)$$

where E is the expected-value operator, δ is the Dirac-delta. Appendix B gives representative values that are used.

The weighting matrices $Q(j\omega)$ and $R(j\omega)$ are selected based on the uncertainties in the system. For the experimental apparatus, the dominant high frequency modelling error results from a fixed time delay of 30ms in the vision system. Consequently, selecting a $Q(j\omega)$ and $R(j\omega)$ that yield a roll-off in the control usage above $5\,Hz$ is sufficient. This can be accomplished by letting $Q(j\omega) = Q = constant$ and letting $R(j\omega)$ increase with frequency as shown in Figure 7.

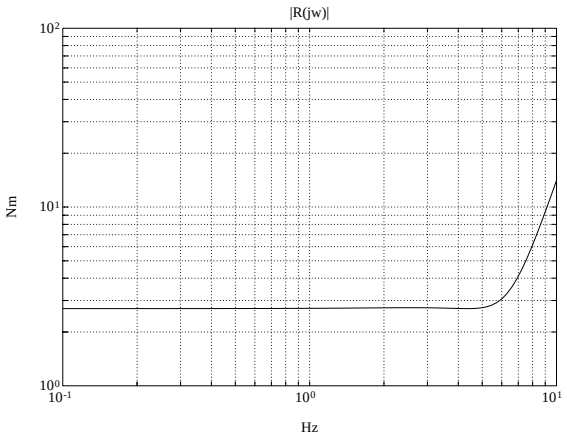

Figure 7: $|\,P(j\omega)\,|$

The actuator weighting matrix is

$$R(j\omega) = P^*(j\omega) P(j\omega).$$

The magnitude of $P(j\omega)$ is shown here. This is the actuator weighting used in all LQG designs.

The control law which minimizes this performance index is of the form

$$u(s) = G_c(s) y_s(s). \quad (10)$$

The actual procedure for minimizing Equation 5 is described in [12]. The frequency weighted cost function is transformed into the time domain yielding a "standard" linear quadratic cost function. The only difference is the presence of augmented states that generate the frequency shaping of the control. The cost function is then minimized assuming full state feedback. The states are estimated using a constant-gain Kalman filter.

Control Design: Rigid Payloads

The frequency-shaped LQG control design technique is first applied for a rigid-body payload configuration. For this case, the controlled outputs are

$$y_c = \begin{bmatrix} Payload\,Position\ \ (Y_p), \\ Payload\,Orientation\ \ (\alpha), \\ Payload\,Orientation\,Rate\ \ (\dot{\alpha}) \end{bmatrix}. \quad (11)$$

The weighting matrices used in the performance index are given in Appendix B, and the process disturbance influence matrix $(,)$ is set equal to the actuator influence matrix (B).

The resulting controller produces a response to a step command in payload position as shown in Figure 8. These are experimental data. The step response has negligible

overshoot and a two second rise time. The bandwidth is effectively two times the fundamental cantilever mode of the arm ($f_{cant} = 0.2$ Hz). The controller is robust to the time delay of 30 ms in the vision system.

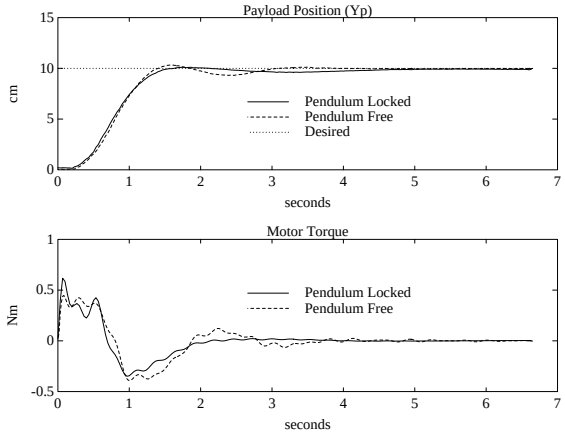

Figure 8: **Step Response**

This shows the response of the system to a step command in the desired payload position. The top plot shows the payload position response; the bottom plot shows the actuator effort. The solid line is for the case of a rigid payload; the dashed line is for the case of a dynamic payload. The controllers are different for the rigid and dynamic payload cases. The controllers here are designed with an accurate payload model.

Control Design: Dynamic Payloads

Next, the robust control technique is applied to a dynamic payload configuration. Note again that the dynamics of the payload are assumed to be known for this discussion. For this case, the outputs weighted in the performance index (not measured) are modified from the rigid payload case (see Equation. 11) to include the internal dynamics of the payload.

$$y_c = \begin{bmatrix} Payload\,Position\ \ (Y_p), \\ Payload\,Orientation\ \ (\alpha), \\ Payload\,Orientation\,Rate\ \ (\dot{\alpha}), \\ Pendulum\,Angle\ \ (\phi), \\ Pendulum\,Angular Velocity\ \ (\dot{\phi}) \end{bmatrix}. \qquad (12)$$

The objective is to design a controller that is capable of controlling the position and orientation of the payload as well as damp the internal motion of the payload. The weighting matrices for the performance index are given in Appendix B.

The resulting controller increases the damping ratio of the pendulum to 5% as compared to less than 0.5% open-loop. Figure 9 shows the response from unknown initial conditions of the pendulum angle. The pendulum damps in 3 seconds as opposed to one minute open loop. The step response was included in Figure 8.

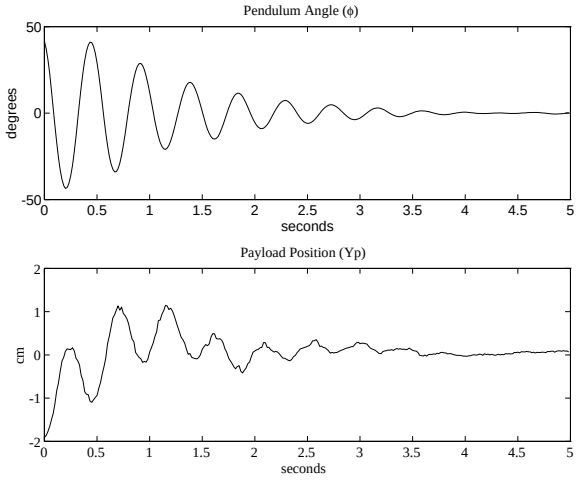

Figure 9: **Pendulum Release**

The pendulum is released from a 45° initial condition. The LQG controller with accurate model of payload is able to quickly regulate the system

The conclusion is that control laws that are robust to the high-frequency uncertainties can be developed if the system equations-of-motion are known over the frequency range that includes the vibrations to be actively controlled. This is true for both the pendulum-free and pendulum-fixed configurations.

Sensitivity to Parameter Error

In a deployed system, accurate models of the payload might not be available. This section demonstrates that the controllers designed above while robust to high-frequency uncertainties are not robust to uncertainties in the payload model. In particular, two cases are examined. First, the controller designed assuming a rigid payload is applied to a system with the pendulum free. Second, a controller designed using an incorrect assumed length of the pendulum is applied.

Case #1:

When a controller that is designed assuming that the pendulum is locked is applied to a system with a dynamic payload, the closed-loop system roots shown in Figure 10 result. Plotted are the root locations in the S-plane versus

pendulum length. This plot indicates that the pole locations that correspond to the rigid-payload modes (represented by the x's on the plot) are somewhat insensitive to the presence of the dynamic payload. However, the pendulum introduces a new lightly damped root which is very sensitive to the length of the pendulum. Further, when the open-loop frequency of this pendulum-dominated mode is near one Hertz, the closed-loop system is unstable.

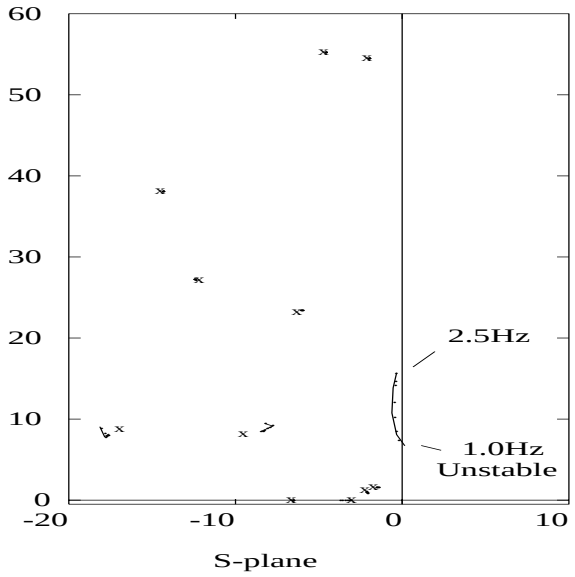

Figure 10: **Roots vs Pend. Frequency**

This figure shows the locus of the closed-loop roots of the system vs the open-loop frequency of the pendulum. The controller is designed for a rigid-body payload. The x's are the location of the closed-loop roots when the payload is rigid. The lines show how the closed-loop roots move as the open-loop frequency of the pendulum is varied from 2.5 to 1.0 Hz

Figure 10 is consistent with the dynamic characteristics discussed in Section 2. The closed-loop roots associated with the primary three system modes are not greatly affected by the presence of payload dynamics. In addition, the pendulum-dominated mode is not well damped. In fact, the controller can cause a slight destabilizing effect on this mode.

In the experimental system, the pendulum open-loop frequency can be varied from 1.5 to 2.5 Hz. Over that range, the observed closed-loop damping ratio is less than 0.5% and is in agreement with Figure 10. Figure 11 shows an experimental time response. Noting the potential for instability, the locus verifies that the payload dynamics cannot be neglected when using end-point control.

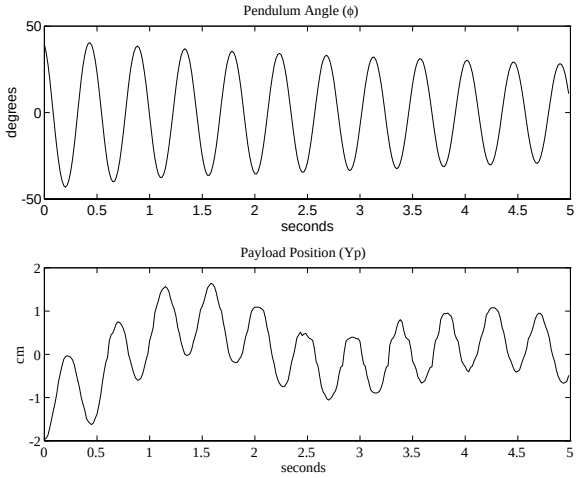

Figure 11: **Pendulum Release**

The pendulum is released from a 45° initial condition. The controller is designed for a rigid-body payload and is unable to control the pendulum inside the payload.

Case #2:

The performance of a controller designed to account for the pendulum is sensitive to the accuracy of the assumed pendulum length. If the assumed length is in error such that the natural frequency of the payload is off by 10%, the system is *unstable*. Thus, the frequency weighted controller while robust to the high-frequency uncertainties is still sensitive to payload dynamic uncertainties.

4 Adaptive Algorithm

The frequency-shaped LQG designs generated above demonstrate that high-performance control is possible, even in the presence of high-frequency uncertainties. However, it was shown that an accurate model of the system was required in the frequency range including the vibration modes that are to be actively controlled. Modelling errors associated with unknown payload dynamics may not satisfy this condition.

In this section, an adaptive control algorithm is presented that merges the robust LQG controllers with a novel identification procedure that is able to provide the model fidelity that is required for precise control. Given this, the performance shown in Figures 8 and 9 is achievable for a range of unknown pendulum lengths in the payload.

The approach presented is based on extensions to the self-tuning-regulator (STR) class of adaptive control. The approach is unique in that (1) it exploits the closed-loop

dynamic characteristics of the class of systems being investigated and (2) it incorporates the first experimental, on-line demonstration of a new identification technique.

The concept of a self-tuning-regulator is presented in Figure 12. It depicts the combination of two functions. First, an identification algorithm is used to update the equations of motion of the plant. Second, a control design algorithm (either gain calculation or scheduling) is used to modify the control law. Details of the basic STR approach are provided in [13].

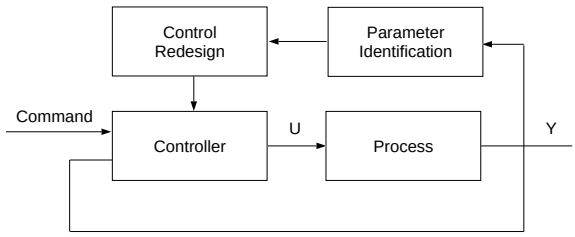

Figure 12: **Self Tuning Regulator**
The parameter identification and control redesign are used to modify the controller so that good performance can be achieved for a variety of plant parameters.

Although in concept the STR is straightforward, there are several issues which must be addressed to achieve a practical implementation. Some of the problems include

1. The identification algorithm must determine the form of the system equations of motion as well as identify the free parameters. In general, the algorithm must determine the order of the system as well as the location of all the poles and zeros (or equivalent parameters of another realization).

2. The identification algorithm must avoid *excessive* excitation of the system. Identification generally improves as the level of excitation increases. However, excessive excitation may be unsafe or undesirable for some situations (e.g., when holding a delicate payload).

3. The identification algorithm must operate sufficiently fast so that the identification can provide an updated set of system equations in a *timely fashion*. That is, the system can be unstable if the nominal control (rigid payload assumed) is operating when there is a pendulum dominated mode present. The identification algorithm must provide an update within a small number of cycles of the pendulum dominated mode.

A solution to these problems for the class of problems under investigation is presented below.

Identification Approach

The procedure employed to develop a viable identification strategy was based on three attributes of the class of systems being studied. The first is that only the set of parameters which describes the payload dynamics is unknown. That is, the parameters that describe the arm are known well enough so that (with no payload attached) the arm's dynamics are well characterized in the frequency range that includes the vibration modes to be controlled. This attribute will be typical of deployed space robotic systems. The consequence of this is that a complete system model can be constructed from an identification of the payload only.

The second attribute is that the structure of the equations of motion of the payload are known. In the general case, nothing about the payload is known apriori. However, for this research the structure of the payload is assumed known. Specifically in the experiment, the payload can be a rigid body or it can include a single pendulum of unknown length. Thus, the identification can be limited to finding a small number of unknown parameters within a known structure.

The third attribute is that a *nominal* control law can be found that yields a set of well-damped closed-loop system modes which have eigenvalues that are relatively insensitive to the presence of payload dynamics. Further, if a pendulum dominated mode is present, it is "near" the $j\omega$ axis[2], and appears in a region of the S-plane that is *remote* from the nominal set of controlled modes (see Figure 10 in Section 3). As a consequence, the existence of payload dynamics can be detected by determining the presence or absence of modal content of the closed-loop system in the critical region of the S-plane only (see Figure 13).

The identification procedure that exploits these features is described in Figure 14. The procedure is split into detection and identification phases. The detection is accomplished by evaluating the modal content (e.g., eigenvalues) of the system while under normal operation (closed loop). The controller that is running during the detection phase is designed assuming the payload is a rigid body (see Section 3). No identification specific inputs are required. When evaluating the modal content, all of the closed-loop eigenvalues might be found, but only the poles within the critical region of the S-plane are of interest (see Figure 13). If a pole appears within the critical region, the payload is known to have internal dynamics. If a pole is not detected in the critical region, then either the pendulum is locked or it is not excited. In either case, it does not need to be controlled. If the pendulum becomes excited, the pole will be detected in the critical region of the S-plane.

[2] i.e., the motion is oscillatory and the amplitude of the oscillations increases or decreases slowly

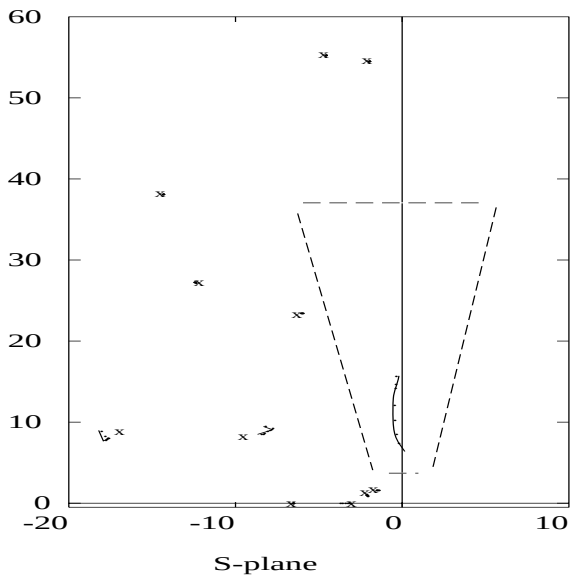

Figure 13: **Critical Region**

The dotted region in the S-plane is the critical region. Once a pole is detected in the critical region, the pendulum is known to exist and its frequency can be determined.

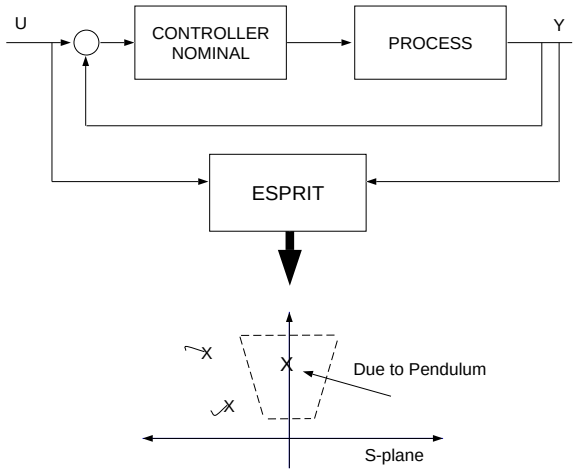

Figure 14: **Closed-Loop Identification**

Performing the identification closed loop allows the poles that are sensitive to the payload dynamics to be isolated.

Once a pole is detected in the critical region, its exact location can be used to identify the unknown parameter (in this case length of the pendulum). For the experimental system under *nominal* control, the location of the critical pole is directly related to the length of the pendulum. In a more general case, there may be more than one mode of the payload and more than one uncertain parameter. If

$\theta \equiv$ vector of the unknown payload parameters

$\lambda \equiv$ closed-loop eigenvalues detected in the critical region

then, for a given system and *nominal* controller, λ is a function of θ.

$$\lambda = f(\theta) \tag{13}$$

In general, if there are fewer unknowns than payload modes, θ can be found using a least squares approach. If this function is invertable, the unknown parameters can be identified from the modes through the inverse of the function. For the experimental system, θ is a scalar. Consequently, the function in Equation 13 can be plotted and inverted graphically. Thus, once the location of the critical pole is determined, the identification of the pendulum length is accomplished using a straightforward table look-up.

Since no identification of θ is performed until a pole is detected in the critical region, the payload is only identified when sufficient excitation exists naturally. There is no need to provide identification specific excitation.

Eigenvalue Identification

The performance of the adaptive logic described above depends heavily on the ability of an identification algorithm to provide accurate estimates of the eigenvalues of the system that appear in the critical region of the S-plane (Figure 13).

The approach for accomplishing this was based on a recently developed subspace fitting identification technique called ESPRIT [14]. ESPRIT is used as linear identification technique that takes as inputs the digitized input and outputs of the system being identified. The algorithm returns a best fit linear state-space model. More precisely, ESPRIT is a new mathematical tool that processes the specific Hankel matrices which Ho, Kalman [15] observed have special properties. Further, ESPRIT adds the ability to account for noise in all measurements. The ESPRIT algorithm is described in detail in Appendix C in the context of linear system identification.

A critical feature of ESPRIT is its ability to identify a system without assuming the order. To determine the order of excited dynamics, ESPRIT forms a matrix, $\mathbf{YU}^{\perp}$ (see Appendix C, Equation 42). The singular values of $\mathbf{YU}^{\perp}$ are a measure of the influence each mode has on the sampled data. If the data were from a true linear system with no noise, the matrix would have the same number of non-zero singular values as there are excited modes of the dynamic system. However, because the data are corrupted with noise, there are many more non-zero

singular values. Figure 15 shows an example plot. By looking at the singular value plot, a *noise floor* can be established (see [11] for details on calculating the *noise floor*). The number of singular values above the *noise floor* is the order of the excited dynamics.

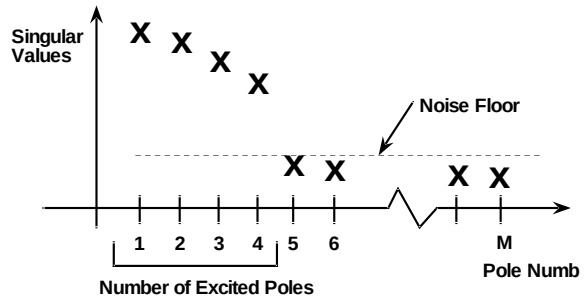

Figure 15: **Singular Values $\mathbf{YU}^{\perp}$**

The large drop in values from the 4th to the 5th singular value indicates that there are 4 excited modes in this example system.

Once the order of the system has been determined, ESPRIT forms a state-space realization of the proper order that best fits the data. Although ESPRIT is capable of identifying a complete linear model of the system (A, B, C_s), it is computationally intensive and requires full excitation to get an accurate model. Experiments show[3] the required excitation and time for identification make an unmodified ESPRIT algorithm inappropriate for real-time adaptive control of this system.

The approach to payload identification described in the above section does not require a complete system model identification (A, B, C_s), however. Since the identification problem can be reduced to a problem of finding eigenvalues in a critical region of the S-plane, only the system matrix, A, is needed. The attribute of ESPRIT that was exploited/developed for this application is that it can be configured to identify only those eigenvalues which are excited with an order of magnitude less computation than finding a complete model of the system dynamics. No special inputs are required since only the excited eigenvalues are being computed.

The Adaptive System

In summary, the identification and control strategies developed in the previous sections can be combined to yield an adaptive system. The payload is first assumed to be rigid, and the *nominal* controller which yields good performance for rigid payloads is used to control the system. The closed-loop system is then monitored for the presence of critical modal content. If the payload is a rigid body, no adaptation occurs. If critical modal content is detected, the parameters of the payload are identified and an appropriate control law is activated. In general, the control law could be computed on-line. For the experimental system, however, it was possible to compute the control gains off-line and schedule them against the single unknown system parameter, pendulum length.

[3] As a test, ESPRIT was used off line to identify the experimental system. A specially designed excitation was necessary to excite all the modes of the system. Nearly thirty seconds of excitation was required to get a good identification. The data took several minutes to process in a batch algorithm.

5 Experimental Results

This section shows the results of three separate tests of the adaptive algorithm on the hardware. For all of these tests, the window size for the identification algorithm was set to two seconds. Each window of data was processed in 0.1 seconds giving an identification update rate of 10 Hz. The sample rate was 60 Hz.

The pendulum drop test , shown in Figure 16, starts with the pendulum mechanically held at a 45^o initial condition so that the payload is initially a rigid body. While the controller is regulating the payload position, the pendulum is released (at 2.2 seconds). For the next two seconds, the pendulum motion is decaying very slowly with a damping ratio of less the 0.5% (see Figure 10). During this time, the identification algorithm detects presence of the pendulum and identifies the frequency of its associated mode. At four seconds into the run, the controller that accounts for the payload dynamics is swapped in. Three seconds later, the pendulum is damped to within five degrees and the arm to within two millimeters of their desired positions.

The disturbance response test, shown in Figure 17, demonstrates the response of the adaptive algorithm to large unmodelled disturbances for both rigid and dynamic payloads. The pendulum is initially locked hanging straight down. An impulsive disturbance is applied to the tip of the manipulator. The controller rejects the disturbance. As expected, no adaptation takes place. This is in contrast to other adaptive algorithms that respond unfavorably to unmodelled disturbances. The pendulum is then released. However, since the pendulum is not oscillating there is no need to identify or control it. A second impulsive disturbance is then applied to the tip of the manipulator. This disturbance excites the pendulum enabling the adaptive algorithm to identify and hence damp the pendulum while simultaneously regulating the payload position. Note that neither the identification nor control algorithm is able to sense the pendulum angle directly (even though it is plotted).

The drop and slew test, shown in Figure 18, shows adaptation during a slew. The idea is similar to the first

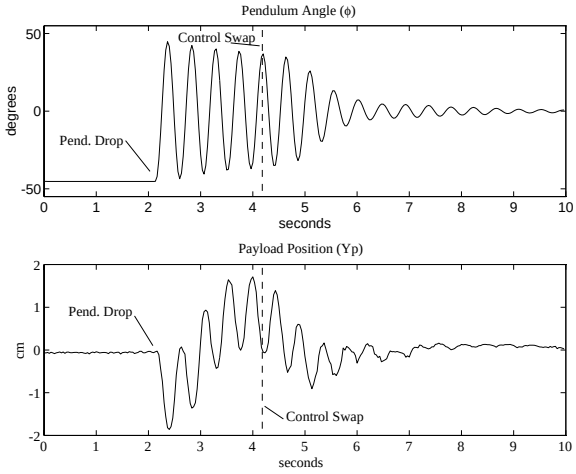

Figure 16: **Adaptive Control: Pendulum Drop**
This experimental result shows the response of the adaptive system when the pendulum is given a 45^o initial condition. After 4 oscillations, the identification has converged and a new controller is swapped in to damp the pendulum.

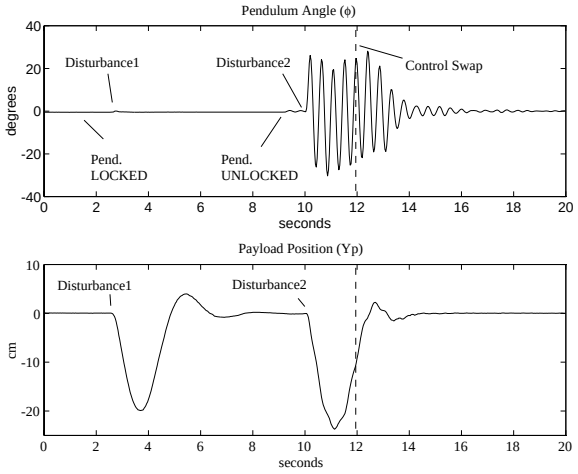

Figure 17: **Disturbance Response**

This experimental result shows the response of the adaptive system to disturbances when the payload is rigid and dynamic. The identification algorithm is not led to false identification by large unmodelled disturbances.

experiment in that the pendulum is initially held at a 45^o initial condition and then dropped. However, this time the pendulum is dropped just as the robot is commanded to slew the payload to a new position on the table. The adaptive algorithm detects and controls the pendulum oscillations while the slew is being completed.

In summary, the three experiments show the response of the system in regulation, disturbance rejection and slew. In all cases the adaptation only occurs when there is excitation of the pendulum. If the pendulum is not excited, the controller will not account for it. Once the pendulum is excited, the algorithm first detects it and then controls it.

6 Conclusions

An effective method for controlling flexible-link robot arms holding payloads with unknown dynamics has been developed and demonstrated experimentally. End-point sensing is used as the primary feedback sensor. The end-point controllers account for high-frequency uncertainties in the plant and parametric uncertainties of the payload. The methodology is to design a controller that is robust to the high-frequency uncertainties, and adapt to the parametric uncertainties.

Robustness to the high-frequency uncertainties is obtained using LQG control with frequency weighting of the cost function. Real-time identification is effectively merged with the robust control in a self-tuning regulator approach to adapt to the parametric uncertainties of the payload. For the class of system presented here, the identification is reduced to determining the modal content of the system under *nominal* control. ESPRIT based algorithms are able to determine accurately and in real-time the modal content of a system without apriori knowledge of the order of the system. Externally supplied excitation is not necessary since the approach does not identify the payload dynamics unless they are first detected from natural excitation.

This approach has proven successful in an experimental demonstration of precise high-bandwidth end-point control with simultaneous damping of internal oscillations of a payload with unknown internal dynamics.

A Equations of Motion

This appendix presents the state space equations of motion for the experimental system. Two cases are presented. The first is for a locked pendulum and the second is for a free pendulum with a fixed length. These two cases correspond to the plots shown in Figure 5. The states are the amplitudes of the mode shapes and their rates.

$$x = \left[\begin{array}{cccccc} q_1 & \dot{q_1} & q_2 & \dot{q_2} & \dots \end{array} \right]^T \tag{14}$$

where q_i is the amplitude of the ith mode shape.

The output matrix, C, is given for the following outputs: hub angle, payload position, payload orientation,

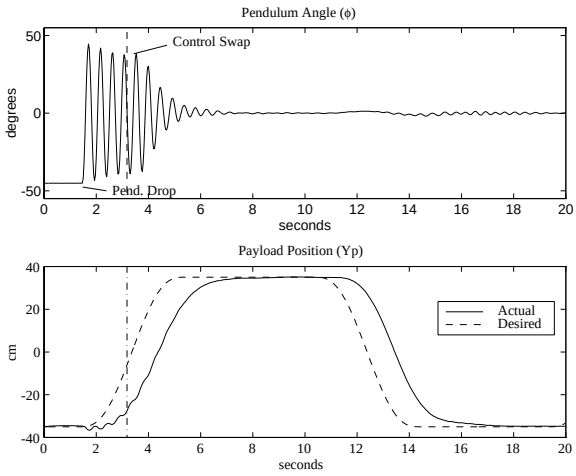

Figure 18: **Drop and Slew**

The pendulum is released from a 45° angle just as the manipulator is commanded to slew. During the slew, the adaptive control identifies and damps the pendulum. The total slew distance is 60cm which sweeps the hub motor through an angle of greater than 40°

pendulum angle (dynamic case only).

Rigid Payload EOM

$$A = diag\left[\begin{array}{cccc} A_{11} & A_{22} & A_{33} & A_{44} \end{array}\right] \quad (15)$$

$$A_{11} = \left[\begin{array}{cc} 0 & 1 \\ 0 & 0 \end{array}\right] \quad (16)$$

$$A_{22} = \left[\begin{array}{cc} 0 & 1 \\ -74.8 & -0.173 \end{array}\right] \quad (17)$$

$$A_{33} = \left[\begin{array}{cc} 0 & 1 \\ -457 & -0.427 \end{array}\right] \quad (18)$$

$$A_{44} = \left[\begin{array}{cc} 0 & 1 \\ -2980 & -3.28 \end{array}\right] \quad (19)$$

$$B = \left[\begin{array}{c} 0 \\ 0.742 \\ 0 \\ 5.53 \\ 0 \\ 5.96 \\ 0 \\ 2.63 \end{array}\right] \quad (20)$$

$$C^T = \left[\begin{array}{ccc} 0.742 & 0.652 & 0.742 \\ 0 & 0 & 0 \\ 5.53 & -0.0755 & -4.294 \\ 0 & 0 & 0 \\ 5.96 & -0.0354 & 5.58 \\ 0 & 0 & 0 \\ 2.63 & 0.0779 & -4.91 \\ 0 & 0 & 0 \end{array}\right] \quad (21)$$

Dynamic Payload EOM

$$A = diag\left[\begin{array}{ccccc} A_{11} & A_{22} & A_{33} & A_{44} & A_{55} \end{array}\right] \quad (22)$$

$$A_{11} = \left[\begin{array}{cc} 0 & 1 \\ 0 & 0 \end{array}\right] \quad (23)$$

$$A_{22} = \left[\begin{array}{cc} 0 & 1 \\ -74.4 & -0.171 \end{array}\right] \quad (24)$$

$$A_{33} = \left[\begin{array}{cc} 0 & 1 \\ -214 & -0.137 \end{array}\right] \quad (25)$$

$$A_{44} = \left[\begin{array}{cc} 0 & 1 \\ -458 & -0.428 \end{array}\right] \quad (26)$$

$$A_{55} = \left[\begin{array}{cc} 0 & 1 \\ -2980 & -3.28 \end{array}\right] \quad (27)$$

$$B = \left[\begin{array}{c} 0 \\ 0.742 \\ 0 \\ 5.51 \\ 0 \\ 7.60 \\ 0 \\ 5.93 \\ 0 \\ 2.63 \end{array}\right] \quad (28)$$

$$C^T = \left[\begin{array}{cccc} 0.742 & 0.652 & 0.742 & 0 \\ 0 & 0 & 0 & 0 \\ 5.51 & -0.054 & -4.24 & -1.63 \\ 0 & 0 & 0 & 0 \\ 0.76 & -0.359 & -0.942 & 27.0 \\ 0 & 0 & 0 & 0 \\ 5.93 & -0.0095 & 5.65 & -1.97 \\ 0 & 0 & 0 & 0 \\ 2.63 & 0.0792 & -4.90 & -.0997 \\ 0 & 0 & 0 & 0 \end{array}\right] \quad (29)$$

B LQG Weighting Matrices

This appendix presents typical values used for the weighting matrices. They were chosen to give good controller performance and do not necessarily model the actual noise spectrum. The weights were chosen using an iterative process. Initially weights were chosen using intuition based on Bryson's rule [16], then the resulting

closed-loop roots and a simulation where used as a guide in adjusting the weights to tune performance.

For the estimator (see equations 3 to 9)

$$Q_n = (5\,Nm)^2 \tag{30}$$

$$R_n = diag\begin{bmatrix} (1\,m)^2 \\ (8\,rad)^2 \\ (400\,rad/sec)^2 \end{bmatrix}. \tag{31}$$

For rigid payloads (see equation 11),

$$Q = diag\begin{bmatrix} (1\,m)^2 \\ (.6\,rad)^2 \\ (.003\,rad/sec)^2 \end{bmatrix}. \tag{32}$$

For dynamic payloads (see equation 12),

$$Q = diag\begin{bmatrix} (1\,m)^2 \\ (.6\,rad)^2 \\ (.003\,rad/sec)^2 \\ (.2\,rad)^2 \\ (.02\,rad/sec)^2 \end{bmatrix}. \tag{33}$$

The actuator weighting matrix is a function of frequency and is shown in figure 7.

C Subspace fitting technique

This appendix describes the subspace fitting technique ESPRIT. ESPRIT is a mathematical tool (three eigendecompositions) for extracting the information from Hankel matrices of impulse response parameters. Ho and Kalman [15] observed that these Hankel matrices have special properties allowing the dimension of an appropriate dynamic model to be obtained. ESPRIT takes into account that there is noise present on all measurements. Reference [14] presents the algorithm in the context of direction of arrival determination for signal processing. The algorithm is presented here in the context of linear system identification.

The subspace fitting technique is inherently digital. Suppose that the system is linear time-invariant as described by the state space model:

$$\mathbf{x}_{k+1} = \mathbf{A}\mathbf{x}_k + \mathbf{B}\mathbf{u}_k \tag{34}$$

$$\mathbf{y}_k = \mathbf{C}\mathbf{x}_k + \mathbf{D}\mathbf{u}_k \tag{35}$$

where $\mathbf{x}_k$ is the state of the linear system at time k, $\mathbf{u}_k$ is the input to the linear system, and $\mathbf{y}_k$ is the observed output ($\mathbf{x}_k \in \Re^{n\times 1}$, $\mathbf{u}_k \in \Re^{q\times 1}$, and $\mathbf{y}_k \in \Re^{m\times 1}$). Since the states are not measured, the system matrices are identifiable only to within an arbitrary non-singular state (similarity) transformation. The identifiability of the system matrices is also limited by the excitation of the system from the inputs or initial conditions.

The algorithm requires a window of data. The length of the data, N, must be selected. A sliding window length size $M \ll N/2$ must also be chosen. The selection of M and N will be discussed later. For now assume they are given.

The first step in the procedure is to take the input and output data and form the following hankel matrices:

$$\mathbf{Y} = \begin{bmatrix} \mathbf{y}_1 & \mathbf{y}_2 & \cdots & \mathbf{y}_{N-M+1} \\ \mathbf{y}_2 & \mathbf{y}_3 & \cdots & \mathbf{y}_{N-M+2} \\ \cdots & \cdots & \cdots & \cdots \\ \mathbf{y}_M & \mathbf{y}_{M+1} & \cdots & \mathbf{y}_N \end{bmatrix} \tag{36}$$

$$\mathbf{U} = \begin{bmatrix} \mathbf{u}_1 & \mathbf{u}_2 & \cdots & \mathbf{u}_{N-M+1} \\ \mathbf{u}_2 & \mathbf{u}_3 & \cdots & \mathbf{u}_{N-M+2} \\ \cdots & \cdots & \cdots & \cdots \\ \mathbf{u}_M & \mathbf{u}_{M+1} & \cdots & \mathbf{u}_N \end{bmatrix} \tag{37}$$

Here

$$\mathbf{Y} = \mathbf{\Gamma}\mathbf{X} + \mathbf{H}\mathbf{U} \tag{38}$$

where,

$$\mathbf{\Gamma}^T = \begin{bmatrix} \mathbf{C}^T & (\mathbf{CA})^T & \cdots & (\mathbf{CA}^{M-1})^T \end{bmatrix} \tag{39}$$

$$\mathbf{X} = \begin{bmatrix} \mathbf{x}_1 & \mathbf{x}_2 & \cdots & \mathbf{x}_{N-M+1} \end{bmatrix} \tag{40}$$

$$\mathbf{H} = \begin{bmatrix} \mathbf{D} & 0 & \cdots & 0 \\ \mathbf{CB} & \mathbf{D} & \cdots & 0 \\ \mathbf{CAB} & \mathbf{CB} & \cdots & 0 \\ \cdots & \cdots & \cdots & \cdots \\ \mathbf{CA}^{M-2}\mathbf{B} & \mathbf{CA}^{M-3}\mathbf{B} & \cdots & \mathbf{D} \end{bmatrix} \tag{41}$$

Thus $\mathbf{Y} \in \Re^{mM\times(N-M+1)}$ and $\mathbf{U} \in \Re^{qM\times(N-M+1)}$, $\mathbf{\Gamma} \in \Re^{mM\times n}$, $\mathbf{X} \in \Re^{n\times(N-M+1)}$, and $\mathbf{H} \in \Re^{mM\times Mq}$. Note that $\mathbf{U}$ and $\mathbf{Y}$ are the only matrices that are formed from measured data.

The second step of the procedure is to find a matrix $\mathbf{U}^\perp$ such that $\mathbf{U}\mathbf{U}^\perp = 0$. $\mathbf{U}^\perp$ can be found from the singular value decomposition of $\mathbf{U}$. Once $\mathbf{U}^\perp$ has been calculated, $\mathbf{Y}\mathbf{U}^\perp$ can be formed from Equation 38. Thus,

$$\mathbf{Y}\mathbf{U}^\perp = \mathbf{\Gamma}\mathbf{X}\mathbf{U}^\perp \tag{42}$$

Note that the column space of $\mathbf{Y}\mathbf{U}^\perp$ is contained in the column space of $\mathbf{\Gamma}$. $\mathbf{\Gamma}$ has n columns. Thus performing a singular value decomposition of $\mathbf{Y}\mathbf{U}^\perp$ should yield n or less non-zero singular values. However, since the data has noise, the last $mM - n$ singular values will not be exactly zero but will be significantly smaller than the first n. The large drop in the singular values of $\mathbf{Y}\mathbf{U}^\perp$ determines the number of excited poles of the system n.

Once the order of the system has been determined, the next step is to find the $\mathbf{A}$ matrix that is of the proper

order that best fits the data. In order to find $\mathbf{A}$, note that the observability matrix $\mathbf{\Gamma}$ possess a shift invariant structure. This means that the second row of $\mathbf{\Gamma}$ can be found by multiplying the first row by $\mathbf{A}$, and the third row can be found by multiplying the second row by $\mathbf{A}$, and so on. However, $\mathbf{\Gamma}$ is unknown. Fortunately, $\mathbf{\Gamma}$ can be computed in a different coordinate system maintaining the shift invariant property. Compute the singular value decomposition of $\mathbf{YU}^{\perp}$:

$$\mathbf{YU}^{\perp} = \mathbf{P\Sigma Q}^T \tag{43}$$

Let $\mathbf{P}_s$ be the matrix containing the first n left singular vectors of $\mathbf{YU}^{\perp}$. It can be shown from Equation 42 and 43 that there exists a full rank $n \times n$ matrix $\mathbf{T}$ such that

$$\mathbf{P}_s = \mathbf{\Gamma}\,\mathbf{T} \tag{44}$$

Expanding the rows of this equation yields,

$$\mathbf{P}_s = \begin{bmatrix} \mathbf{P}_0 \\ \mathbf{P}_1 \\ \mathbf{P}_2 \\ \vdots \\ \mathbf{P}_{M-1} \end{bmatrix} = \begin{bmatrix} \mathbf{C} \\ \mathbf{CA} \\ \mathbf{CA}^2 \\ \vdots \\ \mathbf{CA}^{M-1} \end{bmatrix} \mathbf{T} = \begin{bmatrix} \bar{\mathbf{C}} \\ \bar{\mathbf{C}}\bar{\mathbf{A}} \\ \bar{\mathbf{C}}\bar{\mathbf{A}}^2 \\ \vdots \\ \bar{\mathbf{C}}\bar{\mathbf{A}}^{M-1} \end{bmatrix} \tag{45}$$

So, there is a matrix $\bar{\mathbf{A}}$ which is the state transition matrix of the system in some coordinate frame such that the second row of $\mathbf{P}_s$ can be found by multiplying the first row by $\bar{\mathbf{A}}$, etc. $\mathbf{P}_s$ is $\mathbf{\Gamma}$ in some new coordinate system.

To find $\bar{\mathbf{A}}$, form the following two matrices:

$$\mathbf{P}_{s1} \equiv \mathbf{P}_s \ \textit{with last row deleted} \tag{46}$$

$$\mathbf{P}_{s2} \equiv \mathbf{P}_s \ \textit{with first row deleted} \tag{47}$$

and observe that,

$$\mathbf{P}_{s1}\bar{\mathbf{A}} \approx \mathbf{P}_{s2} \tag{48}$$

The approximation is due to the fact $\mathbf{P}_{s1}$ and $\mathbf{P}_{s2}$ are created from noisy data. $\bar{\mathbf{A}}$ is computed by solving the least squares problem or more accurately the total least squares problem (see [14]) that is posed by Equation 48.

Selecting window size

In order to use the subspace fitting algorithm, one must select the window sizes. The sliding window length window M, and the total window size N are both "design" variables" for the algorithm. One technique for selecting the sliding window length M is to select it such that it captures 1/2 the lowest period signal of interest. The total window size N is usually limited by the computation time. The larger N is the more averaging the algorithm can do and the better the results. However, the svd is an order n^3 operation. N can be selected as large as is computationally reasonable. Recent developments have improved the computational efficiency of the techniques [17].

References

[1] N.C. Singer and W.P. Seering. Preshaping command inputs to reduce system vibration. *Journal of Dynamic Systems, Measurement and Control*, 112(1):76–82, 1990.

[2] E. Bayo, R. Movaghar, and M. Medus. Inverse dynamics of a single-link flexible robot. analytical and experimental results. *International Journal of Robotics and Automation*, 3(3):150–157, 1988.

[3] Robert H. Cannon, Jr. and Eric Schmitz. Initial experiments on the end-point control of a flexible one-link robot. *The International Journal of Robotics Research*, 3(3):62–75, Fall 1984.

[4] Daniel M. Rovner and Robert H. Cannon, Jr. Experiments toward on-line identification and control of a very flexible one-link manipulator. *International Journal of Robotics Research*, 6(4):3–19, Winter 1987.

[5] Daniel M. Rovner and Gene F. Franklin. Experiments in load-adaptive control of a very flexible one-link manipulator. *Automatica*, 24(4):541–548, July 1988.

[6] Anthony P. Tzes and Stephen Yurkovich. Application and comparison of on-line identification methods for flexible manipulator control. *International Journal of Robotics Research*, 10(5):515–527, October 1991.

[7] A.J. Koivo and K.S. Lee. Self-tuning control of a two-link manipulator with a flexible forearm. *The International Journal of Robotics Research*, 11(4):383–395, August 1992.

[8] Sabri Cetinkunt and Sijun Wu. Output predictive adaptive control of a single-link flexible arm. *International Journal of Control*, 53(2):311–333, February 1991.

[9] P. Carton, J.P. Cretien, and M. Maurette. Simulation and control of space manipulators bearing complex payloads. In *Proceedings of XIth IFACS Symposium on Automatic Control in Aerospace*, 1989.

[10] L. J. Alder and S. M. Rock. Control of a flexible robotic manipulator with unknown payload dynamics: Initial experiments. In *Proceedings of the ASME Winter Annual Meeting*, pages 61–66, Atlanta GA, December 1991. ASME.

[11] Lawrence Alder. *Control of a Flexible-Link Robotic Arm Manipulating An Unknown Dynamic Payload.* PhD thesis, Stanford University, Stanford, CA 94305, February 1993. Also published as SUDAAR 632.

[12] Narendra K. Gupta. Frequency-shaped cost functionals: Extension of linear-quadratic-gaussian design methods. *AIAA Journal of Guidance and Control*, 3(6):529–535, November–December 1980.

[13] K. J. Astrom. Theory and applications of adaptive control. In *Proceedings of IFAC Control science and Technology*, pages 737–748, Kyoto, Japan, 1981.

[14] R. H. Roy. **ESPRIT** – *Estimation of Signal Parameters via Rotational Invariance Techniques.* PhD thesis, Stanford University, Stanford, CA., August 1987.

[15] B.L. Ho and R.E. Kalman. Efficient construction o f linear state variable models from input/output functions. *Regelungstechink*, 14:545–548, 1966.

[16] Arthur E. Bryson, Jr. and Yu-Chi Ho. *Applied Optimal Control: Optimization, Estimation, and Control.* Hemisphere Publishing Corporation, 1025 Vermont Ave., N.W., Washington, D.C., 1975. Revised Printing.

[17] Y. Cho, G. Xu, and T. Kailath. On-line identification of state-space models. In *Proceedings of 2nd IFAC Workshop on Algorithms and Architectures for Real-Time Control*, August 1992.